https://doi.org/10.5194/egusphere-2026-81
Preprint. Discussion started: 8 January 2026

Morphology-Conditioned Susceptibility of Marine Stratocumulus Clouds Suggests Weak Cloud Brightening Potential

Tom Goren[1], Goutam Choudhury[1], and Graham Feingold[2]

[1]Department of Environment, Planning and Sustainability, Bar-Ilan University, Ramat Gan, Israel
[2]NOAA, Chemical Sciences Laboratory, Boulder, CO, USA

Correspondence: Tom Goren (tom.goren@biu.ac.il)

Abstract.

We introduce a new framework for defining marine stratocumulus cloud morphologies using a ternary diagram. A ternary diagram is a triangular representation of three components, with each vertex corresponding to 100% of one component, and any point within the triangle representing a mixture of all three that sums to 100%. We use cloud optical thickness (τ_c) as the diagnostic physical variable and accordingly define three corresponding τ_c classes. Different combinations of the three τ_c classes define different cloud morphologies, which vary continuously within the ternary space. The method is applied to one year of satellite observations of stratocumulus clouds and reveals the frequency of occurrence of the different morphologies across the ternary space. Large-eddy simulations complement the satellite analysis and show that cloud evolution tends to follow preferred paths across the ternary morphology space, explaining why the observations are concentrated within a limited range of morphologies. We further investigate the susceptibility of cloud liquid water path (LWP), cloud albedo, and cloud fraction to variations in droplet number concentration, conditioned on cloud morphology. We find that for the most frequent observed morphologies, LWP and cloud albedo susceptibilities largely offset each other, resulting in a net in-cloud albedo response close to zero. The cloud fraction susceptibility is found to be positive in precipitating morphologies and negative in non-precipitating morphologies. These findings have important implications for marine cloud brightening, whose effectiveness needs to be evaluated in a morphology-dependent framework to achieve the intended outcomes.

1 Introduction

Cloud albedo (A_c) is mainly determined by the liquid water path (LWP) and cloud droplet size. To first order these two properties set the cloud optical thickness (τ_c), which is the primary quantity controlling A_c. Aerosols can influence both LWP and droplet size, and thus A_c: An increase in aerosol concentration can raise the cloud droplet concentration (N_d), which reduces droplet size, given no change in cloud water (Twomey, 1974). This results in an increase in A_c. This sensitivity of A_c to N_d is the cloud albedo susceptibility, S_{A_c}. An increase in N_d can also initiate processes that influence the cloud water, which in turn also changes A_c (Ackerman et al., 2004; Albrecht, 1989; Bretherton et al., 2007b). This latter effect, the LWP susceptibility to N_d, S_{LWP}, is termed LWP adjustment, and its sign and magnitude remain uncertain (Glassmeier et al., 2021; Bellouin et al., 2020; Forster et al., 2021; Toll et al., 2019; Goren et al., 2025). Positive LWP adjustments amplify the cloud albedo response to N_d, whereas negative LWP adjustments counteract it. The combined effects of the cloud albedo response and LWP adjustments to changes in N_d determine the net in-cloud albedo susceptibility, S_{net}, which is the quantity that matters for the radiation budget of the Earth.

Cloud albedo varies spatially from meter scales up to hundreds of kilometers (Rampal and Davies, 2020; Stevens et al., 2020; Wood, 2006; Zhou et al., 2021). These spatial variations manifest as different cloud morphologies (Goren et al., 2023; McCoy et al., 2017; Eastman et al., 2024; Wood and Hartmann, 2006; Choudhury and Goren, 2024). Studies that classify stratocumulus cloud morphologies typically define discrete morphology regimes such as open cells, closed cells, and disorganized mesoscale cellular convection (Wood and Hartmann, 2006; Muhlbauer et al., 2014; Erfani and Hosseinpour, 2025; Wu et al., 2025; Yuan et al., 2020; Geiss et al., 2024). Nevertheless, there is a continuum of morphologies between these discrete regime definitions (McCoy et al., 2023; Choudhury and Goren, 2024; Goren et al., 2023), and even fully overcast closed cells, which are typically classified as a single morphology regime, can exhibit structural differences, for example with cells having different horizontal scales (Zhou and Feingold, 2023).

Most studies ignore the dependence of cloud susceptibilities on cloud morphology and instead focus on their dependence on precipitation, cloud fraction (CF), or meteorological conditions (Gryspeerdt et al., 2019; Chen et al., 2025; Hoffmann et al., 2024, 2025; Toll et al., 2019; Glassmeier et al., 2021; Rosenfeld et al., 2019; Zhang et al., 2022). Nevertheless, studies that consider cloud morphology have shown that S_{LWP} varies systematically across different morphologies. Zhou and Feingold (2023), for example, showed that S_{LWP} in closed cells with smaller horizontal extent exhibits values up to ten times larger than in cells with larger horizontal extent. They attributed these differences to entrainment-related evaporation acting within the cell cores versus the cell peripheries. Also S_{A_c} has been shown to depend on morphology, as demonstrated by Goren et al. (2023), who found that S_{A_c} can be positively biased by up to 50% if the spatial distribution of τ_c within a given 1×1 degree scene is ignored.

Here, we introduce a new method for characterizing cloud morphology that provides a continuous, rather than a discrete, classification. Using this framework, we explore fundamental properties of marine low-level cloud morphologies and calculate cloud albedo, LWP, and CF susceptibilities to N_d conditioned on morphology. Section 2 introduces the ternary morphology approach, Section 3 presents the results, and conclusions are given in Section 4.

2 Data and Methods

2.1 Data

Satellite observations of marine low-level clouds over the oceans between 60°N and 60°S in 2015 were selected for the analysis. The observations were taken from the Moderate Resolution Imaging Spectroradiometer (MODIS) Aqua instrument (Platnick et al., 2016), which provides a nadir resolution of 1 km × 1 km. Scenes were filtered to retain only single layer liquid clouds using the MODIS multilayer flag and cloud phase retrieval. Pixels with sensor zenith angles $>55°$ or solar zenith angles $>65°$ were excluded due to retrieval uncertainties (Grosvenor et al., 2018). The satellite retrieved variables used include the corrected reflectance at 0.86 μm, CF (at 5×5 km resolution), LWP, τ_{c}, and cloud top effective radius, r_e. N_{d} was derived from r_e and

τ_c following Grosvenor et al. (2018). The cloud-core LWP was also computed, defined as the mean LWP of the 10% of pixels with the highest LWP within a scene.

To diagnose cloud morphology, one must define an area large enough to capture the relevant morphological scales. For marine low level clouds, morphology scales range from a few tens of kilometers up to about 200 km (Zhou et al., 2021). Following this, the cloud properties of the filtered scenes were gridded onto a uniform 2° × 2° latitude–longitude grid, selected to avoid sampling areas too small to represent the mesoscale cloud morphology. Only scenes with CF > 40% were used in the analysis to avoid broken cloud regimes with their attendant retrieval uncertainties (Choudhury and Goren, 2025; Grosvenor et al., 2018; Wolters et al., 2010). This criterion removes broken cloud regimes with low CF, such as shallow cumulus, sugar, and gravel (Stevens et al., 2020). Figure A1 shows the occurrence of the scenes included in the analysis, which are accordingly found mainly in the stratocumulus regions where closed cells, open cells, and other types of mesoscale cellular convection are common and have relatively higher CF (Muhlbauer et al., 2014). A_c was retrieved from the Clouds and the Earth's Radiant Energy System (CERES) aboard Aqua (Loeb et al., 2005), and gridded to 2° × 2° to match the gridded MODIS data.

Large eddy simulation (LES) output was taken from Goren et al. (2019). The simulations were performed with the System for Atmospheric Modeling (SAM) LES model (Khairoutdinov and Randall, 2003) and were designed to represent a closed-to-open cell transition event observed over the northeast Atlantic Ocean. A full description of the model setup and the simulated case is provided in Goren et al. (2019).

2.2 Methods

2.2.1 Ternary Diagram

A ternary diagram is a triangular graph used to visualize the proportions of three components in a mixture, where each corner of the triangle represents 100% of one component and any point inside represents the relative contributions of all three, which must sum to 100%. In this study, the three components are the fractions of cloudy pixels in three τ_c classes: thin ($\tau_c < 7$), intermediate ($7 \leq \tau_c < 12$), and thick ($\tau_c \geq 12$). The partitioning of τ_c among the three components was done by counting the pixels in each $2°\times2°$ scene whose retrieved τ_c falls into each of the three classes, then normalizing by the total number of pixels with a valid τ_c in the entire scene. Each scene can therefore be represented as a single point in the ternary diagram corresponding to a unique fractional composition of τ_c, which exhibits a unique morphology (see examples in Figure 1).

The ternary space was discretized into evenly sized bins, each representing a unique τ_c morphology. 2° × 2° scenes were assigned to a corresponding morphology bin within the ternary space, and microphysical statistical properties were computed for each bin. Bins containing fewer than 25 scenes were excluded from the analysis and are shown as NaN.

The τ_c class thresholds are defined on physical grounds, based on fundamental radiative transfer considerations: at $\tau_c \approx 7$, A_c transitions from an approximately linear to a more logarithmic dependence on τ_c, and beyond $\tau_c \approx 12$, any further increase in τ_c produces only minimal additional brightening of A_c. We also tested τ_c thresholds of 5 and 10 to align with the common definition of thin clouds as those having $\tau_c < 5$ (McCoy et al., 2023; Wood et al., 2018; Choudhury and Goren, 2024). The results did not change the key findings, and the main difference was a shift in the distribution of scenes within the ternary space.

2.2.2 Decomposing cloud susceptibilities

The ternary framework allows us to estimate cloud susceptibilities to N_d, conditioned on τ_c morphology. We assume that each ternary morphology bin encompasses the natural variability of A_c, N_d, LWP, and CF associated with that bin, and that changes in N_d do not induce transitions between morphology bins. Strong local aerosol perturbations, such as those associated with ship tracks (Goren and Rosenfeld, 2012), can cause shifts between morphology bins, but such perturbations are not considered here. Instead, we focus on the natural variability of background aerosols affecting N_d, which is comparatively smaller. Sensitivity tests in which the bin size was increased to allow greater variability in A_c, N_d, LWP and CF within each bin did not affect the results.

A commonly used approach to estimate S_{LWP} from satellite observations is to regress $d\ln \mathrm{LWP}$ on $d\ln N_d$. However, when LWP and N_d are calculated under the adiabatic assumption using the satellite retrieved τ_c and r_e (Szczodrak et al., 2001), changes in r_e are expected to produce a linear sensitivity of -0.4 between $d\ln \mathrm{LWP}$ and $d\ln N_d$, assuming constant τ_c (Gryspeerdt et al., 2019). This effect was found to dominate S_{LWP} in our analysis (Figure A2) because the variability in τ_c within each ternary bin is relatively small, as each bin is constrained by a τ_c class composition. To avoid this bias, S_{LWP} was calculated by subtracting the theoretical approximation of S_{A_c} (Platnick and Twomey, 1994; Twomey, 1991) from the satellite derived S_{net}. The residual is assumed to be primarily attributable to S_{LWP}, as shown below.

S_{net} (the in-cloud albedo susceptibility) can be written using the chain rule (Bellouin et al., 2020) as:

$$S_{\mathrm{net}} \equiv \frac{d\ln A_c}{d\ln N_d} = \left.\frac{\partial \ln A_c}{\partial \ln N_d}\right|_{\mathrm{LWP}} + \left.\frac{\partial \ln A_c}{\partial \ln \mathrm{LWP}}\right|_{N_d} \frac{d\ln \mathrm{LWP}}{d\ln N_d}. \tag{1}$$

The first term on the right hand side is the cloud albedo response to N_d, S_{A_c} (Twomey, 1991). Using the cloud albedo theoretical approximation (Twomey, 1991; Platnick and Twomey, 1994),

$$S_{A_c} \equiv \left.\frac{\partial \ln A_c}{\partial \ln N_d}\right|_{\mathrm{LWP}} = \frac{1}{3}(1 - A_c), \tag{2}$$

where A_c is the in-cloud albedo of each 2° × 2° scene. S_{A_c} is then averaged to obtain the mean S_{A_c} within each morphology bin, $\overline{S}_{\mathrm{Sc}}$.

$\left.\frac{\partial \ln A_c}{\partial \ln \mathrm{LWP}}\right|_{N_d}$ in equation 1 represents how changes in LWP modify A_c. Because A_c depends primarily on τ_c, and $\tau_c \propto \mathrm{LWP}^{5/6} N_d^{1/3}$ (Platnick and Twomey, 1994; Twomey, 1991), we can write:

$$\gamma \equiv \left.\frac{\partial \ln A_c}{\partial \ln \mathrm{LWP}}\right|_{N_d} = \frac{5}{6}\left.\frac{\partial \ln A_c}{\partial \ln \tau_c}\right|_{N_d} = \frac{5}{6}(1 - A_c) \tag{3}$$

so that equation 1 becomes:

$$S_{\mathrm{net}} \equiv \frac{d\ln A_c}{d\ln N_d} = S_{A_c} + \gamma\,\frac{d\ln \mathrm{LWP}}{d\ln N_d}. \tag{4}$$

For each morphology bin, we estimate S_{net} by regressing the observed $\ln A_c$ on $\ln N_d$ using all scenes within that bin. For consistency with S_{A_c}, we use the bin mean in-cloud albedo, $\overline{A_c}$ in γ, so that $\overline{\gamma} = \frac{5}{6}(1 - \overline{A_c})$. Evaluating equation 1 at each morphology bin gives:

$$S_{\text{net}} = \overline{S}_{\text{A}_\text{c}} + \overline{\gamma}\,\frac{d\ln \text{LWP}}{d\ln N_d}. \tag{5}$$

Solving for S_{LWP} yields S_{LWP} per morphology bin:

$$S_{\text{LWP}} \equiv \frac{d\ln \text{LWP}}{d\ln N_d} = \frac{S_{\text{net}} - \overline{S}_{\text{A}_\text{c}}}{\overline{\gamma}}. \tag{6}$$

S_{CF} was calculated by regressing the observed $\ln(\text{CF})$ on $\ln(N_d)$ for each ternary bin.

3 Results

3.1 Examples of Cloud Morphology Represented in Ternary Space

Figures 1a and 1c show two MODIS swaths containing different cloud morphologies. Figures 1b and 1d show the corresponding $2^\circ \times 2^\circ$ scenes from these swaths mapped onto the ternary diagram. Homogeneous scenes, in which the cellular structure is weakly expressed, are located near the corners of the ternary diagram, whereas inhomogeneous scenes with a more pronounced cellular structure are positioned away from the corners due to their mixed τ_c composition.

The cloud morphology can be seen to vary with CF, cell horizontal scale (large versus small cells), and cloud reflectance, which can differ among cells of similar size. This means that cells with similar horizontal scales can be associated with different morphologies when their scene mean cloud albedo (or τ_c) is different. This extends the study of Zhou and Feingold (2023), which focused on classifying cell morphology by size, by additionally highlighting the role of τ_c variability across cells of similar size. The importance of accounting for τ_c variability was demonstrated also by Goren et al. (2023), who showed that neglecting scene morphology variability can lead to an overestimation of S_{A_c} by up to 50% in the most inhomogeneous scenes.

The morphologies in Figure 1a are predominantly overcast, with homogeneous scenes appearing either as thin stratus layers (red points in Figures 1a and 1b) or as thick closed cells (blue points in Figures 1a and 1b). Between these lie heterogeneous morphologies with stronger contrast between cell cores and their surrounding clouds, reflecting a mixture of τ_c classes.

Figures 1c shows scenes of broken CF and closed cells with larger horizontal extent. These scenes typically correspond to precipitating clouds composed of thick cores ($\tau_c \geq 12$ class) surrounded by a relatively large fraction of thin clouds ($\tau_c < 7$ class) (Wood et al., 2018; O et al., 2018), with only a limited contribution from the moderate τ_c class ($7 \leq \tau_c < 12$). This distinct morphology places these scenes farther toward the left side of the ternary diagram.

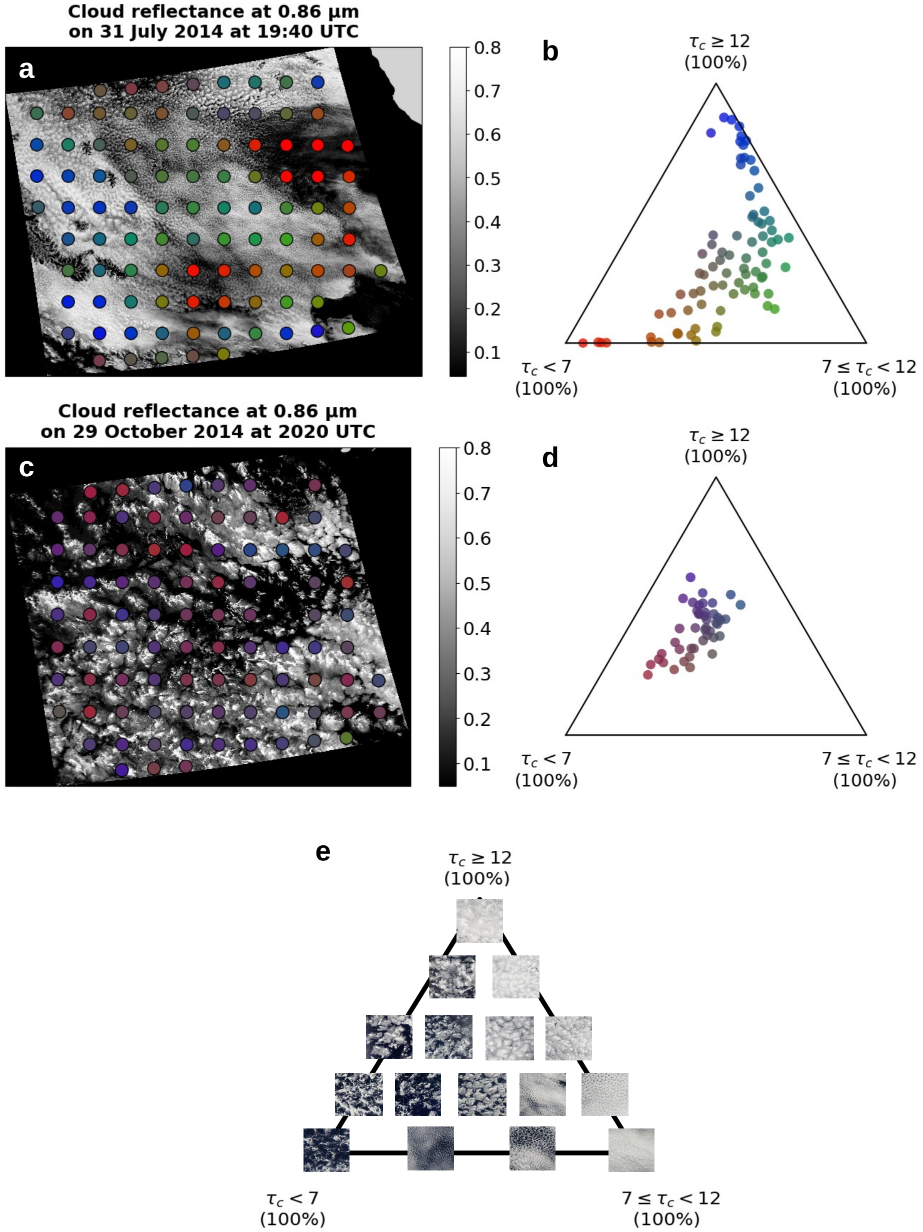

Figure 1. Examples of cloud morphology across the ternary morphology space. A ternary diagram illustrates the relative contributions of three components to a system, where each point represents the fractional contributions of the three components and each corner corresponds to 100% of one component. The ternary corners are defined by τ_c classes: thin clouds ($\tau_c < 7$), intermediate clouds ($7 \leq \tau_c < 12$), and thick clouds ($\tau_c \geq 12$). Panels (a) and (c) show MODIS reflectance at 0.86 μm illustrating different cloud morphologies. Each MODIS swath image is approximately 2330 km wide and 2100 km long. Panels (b) and (d) show the ternary diagram populated with $2° \times 2°$ scenes from the corresponding MODIS swaths in (a) and (c). Colored points represent the fractional contributions of the three τ_c classes as an RGB composite, with red corresponding to $\tau_c < 7$, green to $7 \leq \tau_c < 12$, and blue to $\tau_c \geq 12$. Panel (e) shows MODIS true-color scenes illustrating common cloud morphologies across the ternary space.

3.2 Occurrence of Cloud Morphologies

3.2.1 Observations

Figure 2a shows the 2015 distribution of scenes within the ternary morphology space. The most frequent morphologies are composed of a mixture of homogeneous optically thick and homogeneous optically thin clouds, with a relatively small contribution from the intermediate τ_c class. This implies that most of the variability in scene morphology arises from changes in the relative contributions of the thick and thin τ_c classes, whereas the fractional contribution of the intermediate τ_c class is relatively low. Such a mixtures of τ_c classes characterize active convective cores that coexist with thin clouds diverging from the cloud tops (Wood et al., 2018; Choudhury and Goren, 2024; O et al., 2018). The example in Figures 1c and 1d shows this morphological type, consisting primarily of open cells and disorganized mesoscale cellular convection (Muhlbauer et al., 2014). Similar spatial variability in LWP has been used to distinguish disorganized mesoscale cellular convection from closed and open cells, and from stratus cloud layers with no cellular structure (Wood and Hartmann, 2006; Muhlbauer et al., 2014).

The least frequent morphologies correspond to homogeneous scenes with intermediate τ_c. Interestingly, the scene-mean τ_c of all sampled scenes falls within this τ_c class, with an average value of approximately 9. This means that scene means often reflect a mixture of thick and thin clouds and are therefore not representative of the underlying τ_c distribution. Indeed, Goren et al. (2023) showed that relying on the scene-mean τ_c, rather than accounting for its spatial variability, can lead to a substantial bias in S_{A_c}. Another less frequent morphology appears near the very left side of the ternary, where scenes are dominated by a mixture of thick and thin clouds, with minimal contribution from the intermediate τ_c class.

Figure 2b shows the median CF per ternary bin, revealing a clear separation between overcast and broken scenes. This indicates that overcast and broken scenes are associated with different τ_c morphologies. The highest scene occurrence (Figure 2a) is found for broken cloud morphologies, consistent with previous studies. These scenes are attributed to the high occurrence of disorganized mesoscale cellular convection (Muhlbauer et al., 2014; Goren et al., 2025). The analysis therefore mainly represent stratocumulus clouds, primarily closed and open cells, disorganized mesoscale cellular convection, and stratus layers with no cellular pattern.

3.2.2 Large Eddy simulations

Figures 2c and 2d show the morphology evolution of simulated clouds obtained from a Lagrangian LES of closed cells transitioning to open cells (Goren et al., 2019). The simulated clouds evolve along a morphology trajectory that closely matches the region of highest occurrence in the observations (Figure 2a). This suggests that most observed scenes lie within the stratocumulus morphology evolution space that the analysis is designed to represent.

The simulated evolution of the cloud morphology also provides insight into key cloud processes. One example is cloud thickening during nighttime at the beginning of the simulation, driven by cloud top radiative cooling (Goren et al., 2019). Another is the diurnal cycle in cloud morphology, evident from the daytime loop feature in Figures 2c and 2d. The loop feature shows an increased contribution from the intermediate τ_c class at the expense of the high τ_c class during the daytime morphology evolution (Figure 2c), implying cloud thinning. It is driven by the daytime increase in solar radiation, which

https://doi.org/10.5194/egusphere-2026-81
Preprint. Discussion started: 8 January 2026

leads to cloud thinning and CF reduction (Figure 2d) through warming and evaporation (Hignett, 1991; Meskhidze et al., 2009). Interestingly, the nighttime recovery through cloud thickening follows the same morphological trajectory as the cloud thickening during the previous night, suggesting a preferred evolutionary path. This can explain why the observed cloud morphologies do not span the entire ternary space but instead are concentrated along a preferred region within the morphology space (Figure 2a).

The ternary representation also captures the rapid cloud breakup, indicated by the downward-pointing arrows in Figures 2c and 2d. Because cloud breakup occurs concurrently with the development of substantial precipitation (Goren et al., 2019; Rosenfeld et al., 2006), scenes occupying this morphology space are presumably associated with collision and coalescence processes (Wang and Feingold, 2009).

The above demonstrates that the distribution of scenes within the ternary space encodes information about underlying cloud processes, such as cloud thickening, thinning, and collision–coalescence, which can be inferred from instantaneous satellite snapshots, as shown in Figure 1.

3.3 Cloud Properties Across the Ternary Morphology Space

Figure 3 shows the microphysical properties across the ternary morphology space. In morphology bins characterized by low CF (Figure 2b), N_d is relatively low and r_e exceeds 15 μm (Figure 3a and 3b). This is consistent with precipitation being the primary driver of closed-cell breakup (Rosenfeld et al., 2006; Stevens et al., 2005; Wang and Feingold, 2009; Goren et al., 2019).

An interesting pattern emerges in the LWP field (Figure 3c). High LWP extends from the high τ_c class toward the low τ_c class (thin clouds), along the left side of the ternary. This pattern is somewhat counterintuitive because one might expect high LWP to extend toward the intermediate τ_c class. The reason becomes clear in Figure 3d, which shows the LWP of the cloud cores, defined as the 10% of pixels with the largest LWP. The core LWP is largest along the left side of the ternary, extending toward the lower τ_c class, indicating that the cores remain thick while an increasing fraction of surrounding pixels is gradually replaced by thinner clouds. This morphology is characteristic of stratocumulus in a deep boundary layer, where cloud-top divergence creates thin cloud layers at the top of the boundary layer (Wood et al., 2018; O et al., 2018; Goren et al., 2023; Choudhury and Goren, 2024). It reflects a morphological progression associated with the stratocumulus to cumulus transition (Bretherton and Wyant, 1997; Wyant et al., 1997), consistent with the examples in Figure 1c and 1d, as well as with the simulated closed to open cloud trajectory (Figure 2c and 2d).

At the left corner of the ternary diagram (the $\tau_c < 7$ class), scenes have low LWP. These scenes are associated either with the early stages of stratocumulus formation, typically appearing as an optically thin cloud layer lacking cellular structure (Figure 1a, red points), or with the latest stages of dissipating precipitating cells that leave remnants of thin cloud layers near the top of the boundary layer (Choudhury and Goren, 2024; Wood et al., 2018; O et al., 2018). The simulated morphology evolution further indicates that clouds both form and dissipate near the lowest τ_c class (Figure 3c,d).

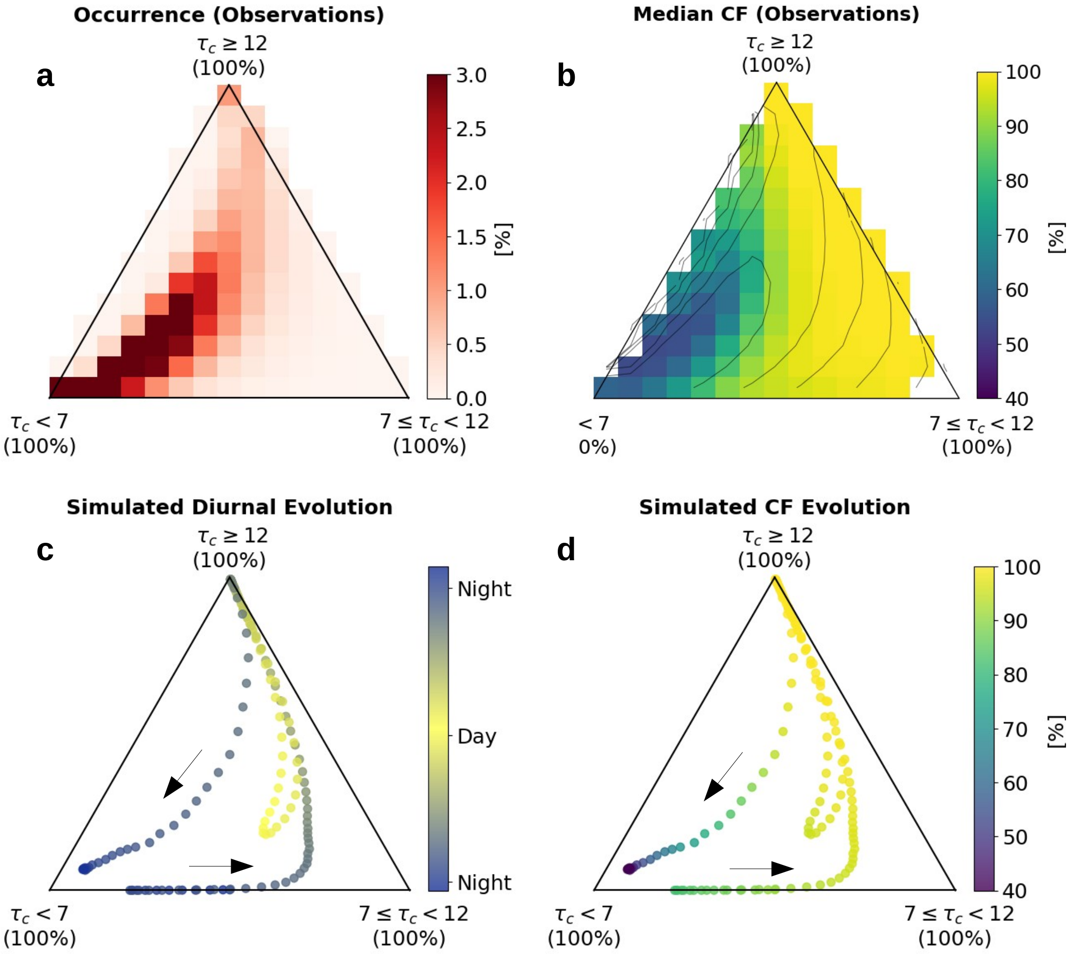

Figure 2. Ternary diagrams of scene occurrence and cloud fraction for satellite observations and LES. (a) Occurrence of 2°×2° scenes from one year (2015) of MODIS Aqua observations of marine low clouds having CF > 40%. Percentages represent the relative contribution of each morphology bin. (b) Median CF for each morphology bin. (c) LES simulation of overcast closed cells transitioning to open cells. (d) Same as (c), but showing CF. Arrows indicate the temporal evolution. The simulated rate of change of the morphology can be inferred from the spacing between successive points.

https://doi.org/10.5194/egusphere-2026-81
Preprint. Discussion started: 8 January 2026

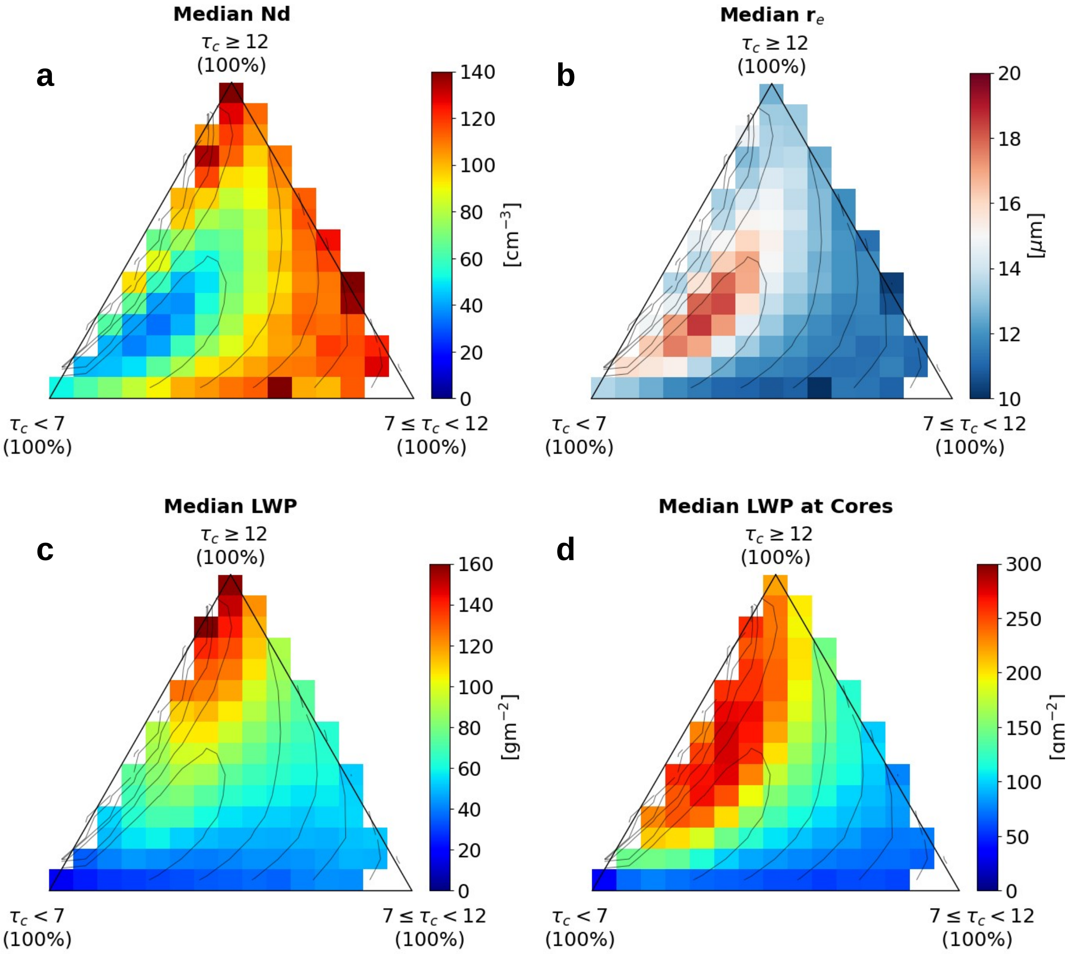

Figure 3. Median ternary-bin values of (a) N_d, (b) r_e, (c) LWP, and (d) cloud-core LWP, defined as the mean LWP of the 10% of pixels with the highest LWP in each scene. Contours indicate scene occurrence (Figure 1a).

https://doi.org/10.5194/egusphere-2026-81
Preprint. Discussion started: 8 January 2026

3.4 Morphology-Conditioned Cloud Susceptibilities

3.4.1 LWP susceptibility

Figure 4a shows that S_{LWP} is negative across the entire ternary space. This contrasts with previous studies that reported both positive and negative S_{LWP}, with the positive values attributed to precipitation suppression (Gryspeerdt et al., 2019; Possner et al., 2020). The negative S_{LWP} indicates that entrainment-related evaporation processes dominate across all morphologies, leading to a reduction in LWP as droplet size decreases with increasing N_d (Bretherton et al., 2007a; Hoffmann et al., 2025; Pincus and Baker, 1994; Wood, 2007). The strongest S_{LWP} of nearly -1 is found in morphology bins where the intermediate τ_c class is dominant. In these scenes the horizontal cell sizes are relatively small (Figure 4a), consistent with Zhou and Feingold (2023), who found similarly strong S_{LWP} in nonprecipitating small closed cells.

S_{LWP} weakens (becomes less negative) as the contribution from the intermediate τ_c class decreases and is replaced by increasing contributions from the lowest and highest τ_c classes. This partly coincides with an increase in r_e to values close to 15 μm (Figure 3b), indicating the presence of precipitation (Rosenfeld et al., 2012), and suggests that precipitation suppression contributes to the weakened S_{LWP}, but not sufficiently to reverse its sign. Our findings are consistent with Goren et al. (2025), who showed that the positive S_{LWP} reported for precipitating scenes in many inverted-V studies (Gryspeerdt et al., 2019; Mülmenstädt et al., 2024; Glassmeier et al., 2021; Possner et al., 2018) does not necessarily reflect precipitation suppression, but can instead arise as an artifact of aggregated sampling across different cloud morphologies.

The weakest S_{LWP} is found in morphologies composed of a mixture of thick and thin τ_c classes, with minimal contribution from the intermediate τ_c class. These morphologies are characterized by relatively large cell sizes (Figure 1c) and r_e close to or exceeding 15 μm (Figure 3), indicating mature closed cells approaching breakup (Goren et al., 2022; Choudhury and Goren, 2024). This is consistent with Zhou and Feingold (2023), who reported weak S_{LWP} for the largest cell sizes. In addition to delayed cloud breakup due to the delayed onset of precipitation, the weak S_{LWP} in these morphologies may also arise from differences in entrainment efficiency between thick cloud cores and the surrounding thin clouds (Zhou and Feingold, 2023; Bretherton et al., 2007b; Kazil et al., 2017). Additionally, the non-negligible contribution of the highest τ_c class indicates the presence of thick, dynamically active cores, as evidenced by the large core-LWP (Figure 1d). These cores likely supply cloud water to the diverging thinner clouds at their tops, which could partially offset LWP losses due to entrainment-driven evaporation, thereby further weakening the negative LWP response.

3.4.2 Cloud albedo susceptibility

Figure 4b shows that the strongest S_{A_c} occurs in the highest τ_c class and extends toward the right corner, where the intermediate τ_c class dominates. The weakest S_{A_c} is found in the lowest τ_c class. This is consistent with the theoretical approximation of S_{A_c} on which the calculation is based, which predicts the largest susceptibility for scenes with $A_c = 0.5$ (Platnick and Twomey, 1994; Twomey, 1991). Figure A3 shows that A_c is indeed around 0.5 in the highest τ_c class.

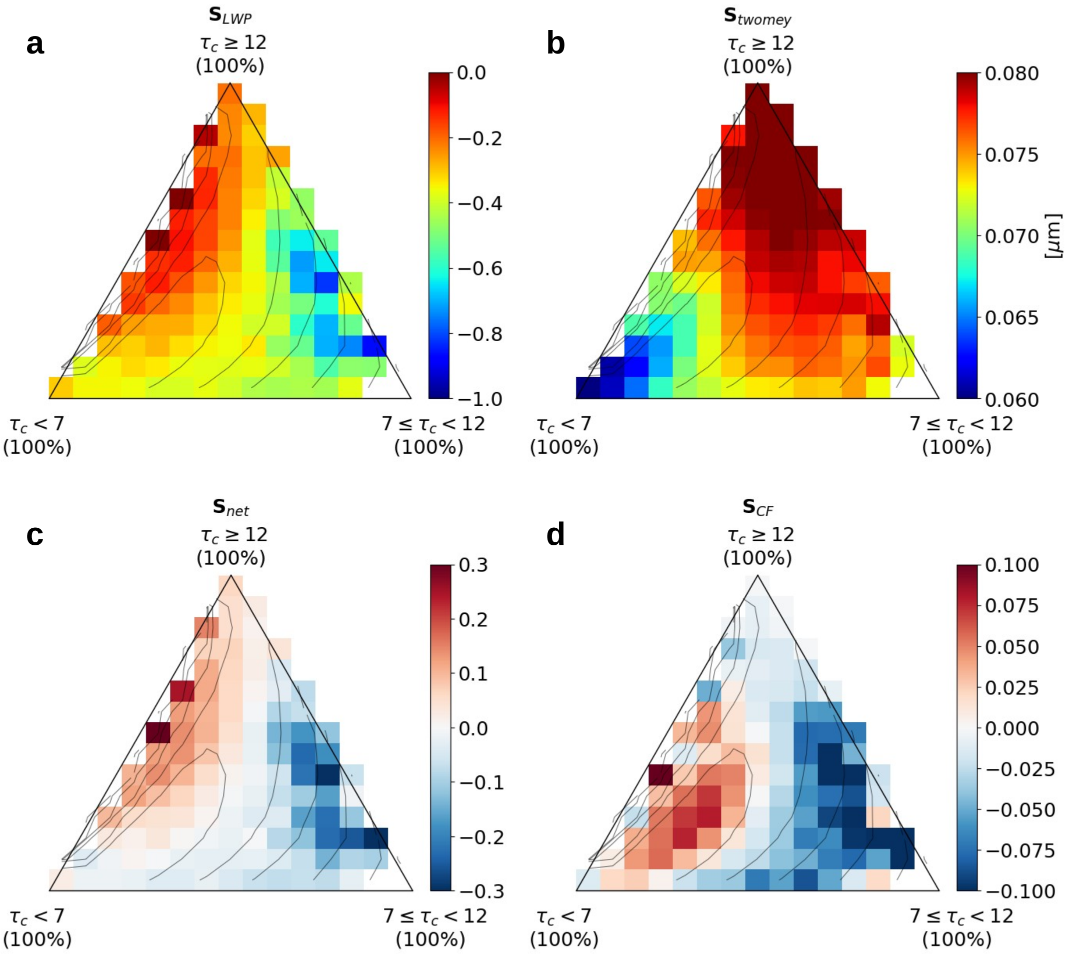

Figure 4. Cloud albedo susceptibility to N_d for (a) LWP, (b) A_c (Twomey effect), (c) net cloud albedo, and (d) CF. Contours represent scene occurrence (Figure 1a).

3.4.3 Net albedo susceptibility

Figure 4c shows a strong dependence of S_{net} on cloud morphology. S_{net} is negative in scenes dominated by intermediate τ_c classes and shifts toward positive values as the morphology becomes dominated by a mixture of thick and thin τ_c classes. The similarity between the morphological dependence of S_{net} and that of S_{LWP} (Figure 4a), together with its lack of similarity to S_{A_c} (Figure 4b), indicates that S_{net} is primarily controlled by S_{LWP}. The strong influence of LWP adjustments on the net albedo response can also be shown theoretically Feingold and Siebert (2009).

The strongest negative S_{net} is found in scenes dominated by the intermediate τ_c class, where S_{LWP} outweighs the relatively strong in-cloud albedo response associated with the Twomey effect, $S_{\mathrm{A_c}}$ (Figure 4b). This is consistent with Zhang et al. (2022), who found that thicker non-precipitating clouds, which likely correspond to the intermediate τ_c class here, exhibit cloud darkening. The strongest positive S_{net}, on the other hand, occurs where S_{LWP} is weakest, that is, least negative (Figure 4a), allowing the Twomey brightening (S_{A_c}) to enhance A_c without being substantially offset by the LWP adjustments.

Both the strongest negative and the strongest positive S_{net} are associated with the least frequent morphologies (Figure 2a), whereas for the most frequent morphologies, S_{LWP} and S_{A_c} approximately balance each other, resulting in S_{net} near zero. As a result, the global mean S_{net} is relatively small, with a value of approximately 0.017. A substantial offset of the Twomey induced brightening by LWP adjustments have been reported also in previous studies (Prabhakaran et al., 2023; Toll et al., 2019; Diamond et al., 2020).

3.4.4 Cloud Cover susceptibility

The LWP and A_c susceptibility analysis focused on in-cloud changes, without considering changes in CF. Here, we further examine S_{CF} (Figure 4d). Positive S_{CF} is found in precipitating scenes, as indicated by $r_e > 15\,\mu\mathrm{m}$ (Figure 3b), consistent with studies reporting a positive relationship between CF and N_d (Rosenfeld et al., 2019; Chen et al., 2014; Wall et al., 2022; Goren and Rosenfeld, 2014). Since stratocumulus breakup is driven by the formation of precipitation (Goren et al., 2019, 2022; Yamaguchi et al., 2017), the positive S_{CF} reflects the effect of increased N_d in slowing precipitation formation, which slows down the reduction of CF.

Negative values of S_{CF}, by contrast, are found in non-precipitating scenes ($r_e < 15, \mu\mathrm{m}$). These scenes are composed primarily of the intermediate τ_c class, where S_{LWP} is strong and negative (Figure 4a). This suggests that the negative strong S_{LWP} drives the negative S_{CF}. The scene-mean LWP in these morphology bins is relatively low (Figure 3c), such that evaporation of cloud water associated with the strong S_{LWP} presumably leads to cloud dissipation and, consequently, a reduction in CF. We assume that the reduction in CF is associated with the thinner clouds at the edges of the cells (see examples in Figure 1e), consistent with the assumptions in Goren and Rosenfeld (2014). The daytime cloud thinning and the associated small reduction in CF shown in Figures 2c and 2c correspond to the negative S_{CF} shown in in Figure 4d, consistent with the reported daytime decrease in CF (Hignett, 1991; Meskhidze et al., 2009). Weak negative S_{CF} are found where scenes are dominated by the thickest τ_c class. In these scenes, clouds are thick and have high LWP, so changes in LWP do not substantially affect scene CF.

4 Conclusions

We have introduced a new method for defining stratocumulus cloud morphologies using a ternary diagram. The ternary is composed of three τ_c classes and provides a continuous morphology space, in contrast to commonly used discrete cloud morphology regime classifications (Wood and Hartmann, 2006; Muhlbauer et al., 2014; Erfani and Hosseinpour, 2025; Wu et al., 2025; Yuan et al., 2020; Geiss et al., 2024). Using one year of satellite observations, we quantify the occurrence of scenes across the morphology space, revealing a preference for a confined range of morphologies. Complemented by LES, we show that cloud morphology evolution follows a preferred path across the ternary morphology space, explaining why most observations fall within a confined range of morphologies. The ternary framework also reveals insights into cloud processes associated with morphology changes, including cloud thickening, the diurnal cycle, and cloud breakup driven by precipitation.

This suggests that the ternary encodes information about cloud processes that can be inferred from instantaneous satellite snapshots (Feingold et al., 2025).

The ternary framework allows us to estimate the susceptibilities of LWP, CF, and A_c to N_d, conditioned on cloud morphology. S_{LWP} is found to be negative across all morphologies, including in precipitating ones, in contrast to studies that have reported positive S_{LWP} and attributed it to precipitation suppression (Dipu et al., 2022; Glassmeier et al., 2021; Gryspeerdt et al., 2019; Mülmenstädt et al., 2024; Possner et al., 2020). Our results support Goren et al. (2025), who showed that the positive S_{LWP} inferred from inverted-V joint histograms of LWP and N_d arises as an artifact of aggregated sampling across different cloud morphologies. S_{CF} is found to be positive in precipitating scenes, presumably because increased N_d delays precipitation and, consequently, cloud breakup (Goren et al., 2019; Wang and Feingold, 2009; Yamaguchi et al., 2017). On the other hand, in non-precipitating scenes with low LWP, S_{CF} is found to be negative, presumably because the strong negative S_{LWP} in these scenes reduces CF through entrainment-related evaporation processes.

The net in-cloud albedo susceptibility (S_{net}) is the most relevant for the radiation budget because it includes the combined contributions of cloud albedo and LWP susceptibilities. S_{net} is found to vary between -0.3 and 0.3 depending on cloud morphology, largely modulated by the strong control of S_{LWP}. Over the most common morphologies, however, it is found to be small, with an occurrence-weighted average of 0.015. This implies that a 10% increase in N_d would result in an increase in cloud albedo of approximately 0.15%, not accounting for changes in CF. Therefore, marine cloud brightening will have to rely on persistent, positive S_{CF} if it is to succeed.

The results presented here have important implications for marine cloud brightening, which should be evaluated in a morphology-dependent manner. The results are also relevant for assessments of cloud radiative forcing due to aerosol–cloud interactions, which should be estimated using morphology-weighted averages.

Data availability. All data sets used in this work are open source. The MODIS aqua cloud products are available from the Atmosphere Archive and Distribution System (LAADS) Distributed Active Archive Center (DAAC): https://ladsweb.modaps.eosdis.nasa.gov/archive/allData/61/MOD06_L2/. CERES radiation data can be accessed at https://ceres.larc.nasa.gov/data/ (last accessed on January 8, 2026). ERA5 pressure level data were obtained from Copernicus Climate Change Service (C3S) Climate Data Store accessible at https://cds.climate.copernicus.eu/.

https://doi.org/10.5194/egusphere-2026-81
Preprint. Discussion started: 8 January 2026

Appendix A: Additional Figures

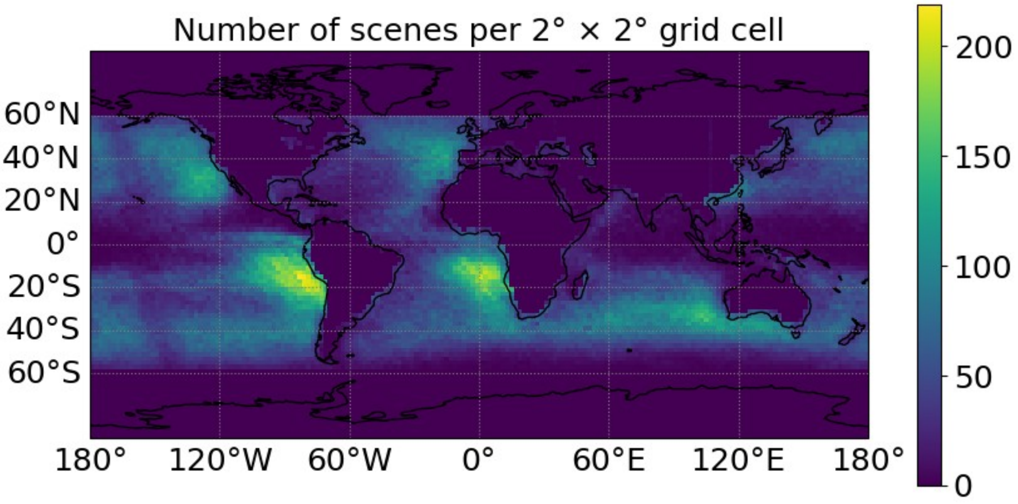

Figure A1. Number of scenes per $2^\circ \times 2^\circ$ grid cell used in the analysis. It can be seen that most scenes derive from the stratocumulus regions in the eastern subtropical oceans.

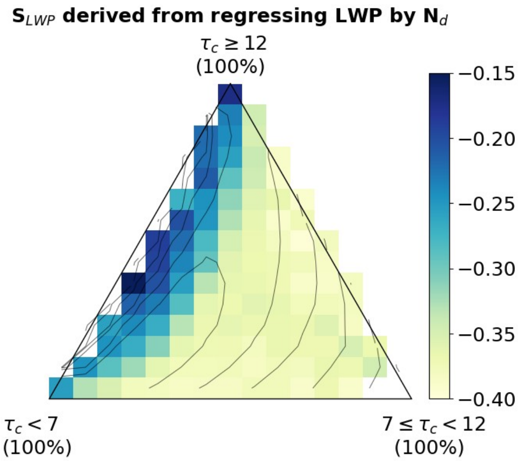

Figure A2. LWP susceptibility derived from the regression between $\ln \mathrm{LWP}$ and $\ln N_d$ within each ternary bin. Contours represent scene occurrence (Figure 2a).

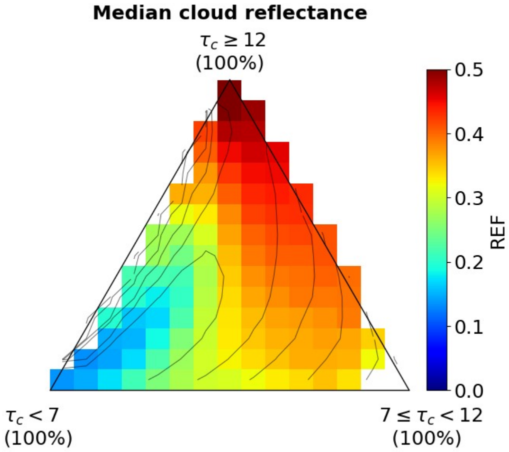

Figure A3. Median ternary-bin values of cloud reflectance at 0.84 μm. Contours indicate scene occurrence (Figure 2).

Author contributions. TG conceptualized the research idea, carried out the study, and wrote the manuscript. GC preprocessed the datasets used in the analysis. All authors contributed to discussions and to the writing of the manuscript.

Competing interests. At least one of the authors is a member of the editorial board of Atmospheric Chemistry and Physics.

Acknowledgements. This work has received funding from the Israel Science Foundation (grant number 3171/24), the United States - Israel Binational Science Foundation (BSF) (grant number 2024152) and the German Research Foundation (Deutsche Forschungsgemeinschaft, DFG; grant number 524386224). G.F. acknowledges support from the NOAA Earth's Radiation Budget Grant #03-01-07-001.

References

Ackerman, A. S., Kirkpatrick, M. P., Stevens, D. E., and Toon, O. B.: The impact of humidity above stratiform clouds on indirect aerosol climate forcing, Nature, 432, 1014–1017, https://doi.org/10.1038/nature03174, 2004.

Albrecht, B. A.: Aerosols, cloud microphysics, and fractional cloudiness, Science, 245, 1227–1230, 1989.

Bellouin, N., Quaas, J., Gryspeerdt, E., Kinne, S., Stier, P., Watson-Parris, D., Boucher, O., Carslaw, K. S., Christensen, M., Daniau, A.-L., et al.: Bounding global aerosol radiative forcing of climate change, Reviews of Geophysics, 58, e2019RG000 660, 2020.

Bretherton, C., Blossey, P. N., and Uchida, J.: Cloud droplet sedimentation, entrainment efficiency, and subtropical stratocumulus albedo, Geophysical research letters, 34, 2007a.

Bretherton, C. S. and Wyant, M. C.: Moisture transport, lower-tropospheric stability, and decoupling of cloud-topped boundary layers, Journal of Atmospheric Sciences, 54, 148–167, 1997.

Bretherton, C. S., Blossey, P. N., and Uchida, J.: Cloud droplet sedimentation, entrainment efficiency, and subtropical stratocumulus albedo, Geophysical Research Letters, 34, L03 813, https://doi.org/10.1029/2006GL027648, 2007b.

Chen, Y.-c., Christensen, M. W., Stephens, G. L., and Seinfeld, J. H.: Satellite-based estimate of global aerosol–cloud radiative forcing by marine warm clouds, Nature Geoscience, 7, 643–646, https://doi.org/10.1038/ngeo2214, 2014.

Chen, Y.-S., Prabhakaran, P., Hoffmann, F., Kazil, J., Yamaguchi, T., and Feingold, G.: Magnitude and timescale of liquid water path adjustments to cloud droplet number concentration perturbations for nocturnal non-precipitating marine stratocumulus, Atmospheric Chemistry and Physics, 25, 6141–6159, 2025.

Choudhury, G. and Goren, T.: Thin clouds control the cloud radiative effect along the Sc-Cu transition, Journal of Geophysical Research: Atmospheres, 129, e2023JD040 406, 2024.

Choudhury, G. and Goren, T.: Sampling bias from satellite retrieval failures of cloud properties and its implications for aerosol-cloud interactions, Geophysical Research Letters, 52, e2025GL115 429, 2025.

Diamond, M. S., Director, H. M., Eastman, R., Possner, A., and Wood, R.: Substantial cloud brightening from shipping in subtropical low clouds, AGU Advances, 1, e2019AV000 111, 2020.

Dipu, S., Schwarz, M., Ekman, A. M., Gryspeerdt, E., Goren, T., Sourdeval, O., Mülmenstädt, J., and Quaas, J.: Exploring satellite-derived relationships between cloud droplet number concentration and liquid water path using a large-domain large-eddy simulation, 2022.

Eastman, R., McCoy, I. L., Schulz, H., and Wood, R.: A survey of radiative and physical properties of North Atlantic mesoscale cloud morphologies from multiple identification methodologies, Atmospheric Chemistry and Physics, 24, 6613–6634, 2024.

Erfani, E. and Hosseinpour, F.: A Novel Approach for Reliable Classification of Marine Low Cloud Morphologies with Vision–Language Models, Atmosphere, 16, 1252, 2025.

Feingold, G. and Siebert, H.: Cloud–aerosol interactions from the micro to the cloud scale, in: Clouds in the Perturbed Climate System: Their Relationship to Energy Balance, Atmospheric Dynamics, and Precipitation, edited by Heintzenberg, J. and Charlson, R. J., pp. 319–338, MIT Press, Cambridge, Massachusetts, 2009.

Feingold, G., Glassmeier, F., Zhang, J., and Hoffmann, F.: Opinion: Inferring process from snapshots of cloud systems, Atmospheric Chemistry and Physics, 25, 10 869–10 885, 2025.

Forster, P., Storelvmo, T., Armour, K., Collins, W., Dufresne, J.-L., Frame, D., Lunt, D., Mauritsen, T., Palmer, M., Watanabe, M., Wild, M., and Zhang, H.: Chapter 7: The Earth's energy budget, climate feedbacks, and climate sensitivity, https://doi.org/10.25455/wgtn.16869671, 2021.

Geiss, A., Christensen, M. W., Varble, A. C., Yuan, T., and Song, H.: Self-supervised cloud classification, Artificial Intelligence for the Earth Systems, 3, e230 036, 2024.

Glassmeier, F., Hoffmann, F., Johnson, J. S., Yamaguchi, T., Carslaw, K. S., and Feingold, G.: Aerosol-cloud-climate cooling overestimated by ship-track data, Science, 371, 485–489, 2021.

Goren, T. and Rosenfeld, D.: Satellite observations of ship emission induced transitions from broken to closed cell marine stratocumulus over large areas, Journal of Geophysical Research: Atmospheres, 117, https://doi.org/10.1029/2012JD017981, 2012.

Goren, T. and Rosenfeld, D.: Decomposing aerosol cloud radiative effects into cloud cover, liquid water path and Twomey components in marine stratocumulus, Atmos. Res., 138, 378–393, https://doi.org/10.1016/j.atmosres.2013.12.008, 2014.

Goren, T., Kazil, J., Hoffmann, F., Yamaguchi, T., and Feingold, G.: Anthropogenic air pollution delays marine stratocumulus breakup to open cells, Geophysical Research Letters, 46, 14 135–14 144, 2019.

Goren, T., Feingold, G., Gryspeerdt, E., Kazil, J., Kretzschmar, J., Jia, H., and Quaas, J.: Projecting stratocumulus transitions on the albedo—cloud fraction relationship reveals linearity of albedo to droplet concentrations, Geophysical Research Letters, 49, e2022GL101 169, 2022.

Goren, T., Sourdeval, O., Kretzschmar, J., and Quaas, J.: Spatial aggregation of satellite observations leads to an overestimation of the radiative forcing due to aerosol-cloud interactions, Geophysical Research Letters, 50, e2023GL105 282, 2023.

Goren, T., Choudhury, G., Kretzschmar, J., and McCoy, I.: Co-variability drives the inverted-V sensitivity between liquid water path and droplet concentrations, Atmospheric Chemistry and Physics, 25, 3413–3423, 2025.

Grosvenor, Sourdeval, O., Zuidema, P., Ackerman, A., Alexandrov, M. D., Bennartz, R., Boers, R., Cairns, B., Chiu, J. C., Christensen, M., Deneke, H., Diamond, M., Feingold, G., Fridlind, A., Hünerbein, A., Knist, C., Kollias, P., Marshak, A., McCoy, D., Merk, D., Painemal, D., Rausch, J., Rosenfeld, D., Russchenberg, H., Seifert, P., Sinclair, K., Stier, P., van Diedenhoven, B., Wendisch, M., Werner, F., Wood, R., Zhang, Z., and Quaas, J.: Remote Sensing of Droplet Number Concentration in Warm Clouds: A Review of the Current State of Knowledge and Perspectives, Reviews of Geophysics, 56, 409–453, https://doi.org/10.1029/2017RG000593, 2018.

Gryspeerdt, E., Goren, T., Sourdeval, O., Quaas, J., Mülmenstädt, J., Dipu, S., Unglaub, C., Gettelman, A., and Christensen, M.: Constraining the aerosol influence on cloud liquid water path, Atmospheric Chemistry and Physics, 19, 5331–5347, 2019.

Hignett, P.: Observations of diurnal variation in a cloud-capped marine boundary layer, Journal of Atmospheric Sciences, 48, 1474–1482, 1991.

Hoffmann, F., Glassmeier, F., and Feingold, G.: The Impact of Aerosol on Cloud Water: A Heuristic Perspective, Zenodo [data set], 2024.

Hoffmann, F., Chen, Y.-S., and Feingold, G.: On the processes determining the slope of cloud water adjustments in weakly and non-precipitating stratocumulus, Atmospheric Chemistry and Physics, 25, 8657–8670, 2025.

Kazil, J., Yamaguchi, T., and Feingold, G.: Mesoscale organization, entrainment, and the properties of a closed-cell stratocumulus cloud, Journal of Advances in Modeling Earth Systems, 9, 2214–2229, https://doi.org/10.1002/2017MS001072, 2017.

Khairoutdinov, M. F. and Randall, D. A.: Cloud resolving modeling of the ARM summer 1997 IOP: Model formulation, results, uncertainties, and sensitivities, Journal of the Atmospheric Sciences, 60, 607–625, 2003.

Loeb, N. G., Kato, S., Loukachine, K., and Manalo-Smith, N.: Angular distribution models for top-of-atmosphere radiative flux estimation from the Clouds and the Earth's Radiant Energy System instrument on the Terra satellite. Part I: Methodology, Journal of Atmospheric and Oceanic Technology, 22, 338–351, 2005.

McCoy, I. L., Wood, R., and Fletcher, J. K.: Identifying Meteorological Controls on Open and Closed Mesoscale Cellular Convection Associated with Marine Cold Air Outbreaks, Journal of Geophysical Research: Atmospheres, 122, 11,678–11,702, https://doi.org/10.1002/2017JD027031, 2017.

McCoy, I. L., McCoy, D. T., Wood, R., Zuidema, P., and Bender, F. A.-M.: The Role of Mesoscale Cloud Morphology in the Shortwave Cloud Feedback, Geophysical Research Letters, 50, e2022GL101 042, https://doi.org/10.1029/2022GL101042, 2023.

Meskhidze, N., Remer, L., Platnick, S., Negrón Juárez, R., Lichtenberger, A., and Aiyyer, A.: Exploring the differences in cloud properties observed by the Terra and Aqua MODIS Sensors, Atmospheric Chemistry and Physics, 9, 3461–3475, 2009.

Muhlbauer, A., McCoy, I. L., and Wood, R.: Climatology of stratocumulus cloud morphologies: Microphysical properties and radiative effects, Atmospheric Chemistry and Physics, 14, 6695–6716, https://doi.org/10.5194/acp-14-6695-2014, 2014.

Mülmenstädt, J., Gryspeerdt, E., Dipu, S., Quaas, J., Ackerman, A. S., Fridlind, A. M., Tornow, F., Bauer, S. E., Gettelman, A., Ming, Y., et al.: General circulation models simulate negative liquid water path–droplet number correlations, but anthropogenic aerosols still increase simulated liquid water path, Atmospheric Chemistry and Physics, 24, 7331–7345, 2024.

O, K.-T., Wood, R., and Bretherton, C. S.: Ultraclean layers and optically thin clouds in the stratocumulus-to-cumulus transition. Part II: Depletion of cloud droplets and cloud condensation nuclei through collision–coalescence, Journal of the Atmospheric Sciences, 75, 1653–1673, 2018.

Pincus, R. and Baker, M. B.: Effect of precipitation on the albedo susceptibility of clouds in the marine boundary layer, Nature, 372, 250–252, 1994.

Platnick, S. and Twomey, S.: Determining the susceptibility of cloud albedo to changes in droplet concentration with the Advanced Very High Resolution Radiometer, Journal of Applied Meteorology and Climatology, 33, 334–347, 1994.

Platnick, S., Meyer, K. G., King, M. D., Wind, G., Amarasinghe, N., Marchant, B., Arnold, G. T., Zhang, Z., Hubanks, P. A., Holz, R. E., et al.: The MODIS cloud optical and microphysical products: Collection 6 updates and examples from Terra and Aqua, IEEE Transactions on Geoscience and Remote Sensing, 55, 502–525, 2016.

Possner, A., Wang, H., Wood, R., Caldeira, K., and Ackerman, T. P.: The efficacy of aerosol–cloud radiative perturbations from near-surface emissions in deep open-cell stratocumuli, Atmospheric Chemistry and Physics, 18, 17 475–17 488, 2018.

Possner, A., Eastman, R., Bender, F., and Glassmeier, F.: Deconvolution of boundary layer depth and aerosol constraints on cloud water path in subtropical stratocumulus decks, Atmospheric Chemistry and Physics, 20, 3609–3621, 2020.

Prabhakaran, P., Hoffmann, F., and Feingold, G.: Evaluation of pulse aerosol forcing on marine stratocumulus clouds in the context of marine cloud brightening, Journal of the Atmospheric Sciences, 80, 1585–1604, 2023.

Rampal, N. and Davies, R.: On the factors that determine boundary layer albedo, Journal of Geophysical Research: Atmospheres, 125, e2019JD032 244, 2020.

Rosenfeld, D., Kaufman, Y. J., and Koren, I.: Switching cloud cover and dynamical regimes from open to closed Benard cells in response to the suppression of precipitation by aerosols, Atmospheric Chemistry and Physics, 6, 2503–2511, https://doi.org/10.5194/acp-6-2503-2006, 2006.

Rosenfeld, D., Wang, H., and Rasch, P. J.: The roles of cloud drop effective radius and LWP in determining rain properties in marine stratocumulus, Geophysical Research Letters, 39, https://doi.org/10.1029/2012GL052028, 2012.

Rosenfeld, D., Zhu, Y., Wang, M., Zheng, Y., Goren, T., and Yu, S.: Aerosol-driven droplet concentrations dominate coverage and water of oceanic low-level clouds, Science, 363, eaav0566, 2019.

https://doi.org/10.5194/egusphere-2026-81
Preprint. Discussion started: 8 January 2026

Stevens, B., Vali, G., Comstock, K., Wood, R., Van Zanten, M. C., Austin, P. H., Bretherton, C. S., and Lenschow, D. H.: Pockets of Open Cells and Drizzle in Marine Stratocumulus, Bull. Am. Meteorol. Soc., 86, 51–57, https://doi.org/10.1175/BAMS-86-1-51, 2005.

Stevens, B., Bony, S., Brogniez, H., Hentgen, L., Hohenegger, C., Kiemle, C., L'Ecuyer, T. S., Naumann, A. K., Schulz, H., Siebesma, P. A., et al.: Sugar, gravel, fish and flowers: Mesoscale cloud patterns in the trade winds, Quarterly Journal of the Royal Meteorological Society, 146, 141–152, 2020.

Szczodrak, M., Austin, P. H., and Krummel, P. B.: Variability of Optical Depth and Effective Radius in Marine Stratocumulus Clouds, Journal of the Atmospheric Sciences, 58, 2912–2926, https://doi.org/10.1175/1520-0469(2001)058<2912:VOODAE>2.0.CO;2, 2001.

Toll, V., Christensen, M., Quaas, J., and Bellouin, N.: Weak average liquid-cloud-water response to anthropogenic aerosols, Nature, 572, 51–55, 2019.

Twomey, S.: Pollution and the planetary albedo, Atmospheric Environment (1967), 8, 1251–1256, 1974.

Twomey, S.: Aerosols, clouds and radiation, Atmospheric Environment. Part A. General Topics, 25, 2435–2442, 1991.

Wall, C. J., Norris, J. R., Possner, A., McCoy, D. T., McCoy, I. L., and Lutsko, N. J.: Assessing effective radiative forcing from aerosol–cloud interactions over the global ocean, Proceedings of the National Academy of Sciences, 119, e2210481 119, 2022.

Wang, H. and Feingold, G.: Modeling Mesoscale Cellular Structures and Drizzle in Marine Stratocumulus. Part I: Impact of Drizzle on the Formation and Evolution of Open Cells, Journal of the Atmospheric Sciences, 66, 3237–3256, https://doi.org/10.1175/2009JAS3022.1, 2009.

Wolters, E. L., Deneke, H. M., van den Hurk, B. J., Meirink, J. F., and Roebeling, R. A.: Broken and inhomogeneous cloud impact on satellite cloud particle effective radius and cloud-phase retrievals, Journal of Geophysical Research: Atmospheres, 115, 2010.

Wood, R.: Relationships between optical depth, liquid water path, droplet concentration, and effective radius in adiabatic layer cloud, University of Washington, 3, 2006.

Wood, R.: Cancellation of Aerosol Indirect Effects in Marine Stratocumulus through Cloud Thinning, Journal of the Atmospheric Sciences, 64, 2657–2669, https://doi.org/10.1175/JAS3942.1, 2007.

Wood, R. and Hartmann, D. L.: Spatial Variability of Liquid Water Path in Marine Low Cloud: The Importance of Mesoscale Cellular Convection, Journal of Climate, 19, 1748–1764, https://doi.org/10.1175/JCLI3702.1, 2006.

Wood, R., O, K.-T., Bretherton, C. S., Mohrmann, J., Albrecht, B. A., Zuidema, P., Ghate, V., Schwartz, C., Eloranta, E., Glienke, S., et al.: Ultraclean layers and optically thin clouds in the stratocumulus-to-cumulus transition. Part I: Observations, Journal of the Atmospheric Sciences, 75, 1631–1652, 2018.

Wu, Y., Liu, J., Zhu, Y., Zhang, Y., Cao, Y., Huang, K.-E., Zheng, B., Wang, Y., Li, Y., Wang, Q., et al.: A global classification dataset of daytime and nighttime marine low-cloud mesoscale morphology based on deep-learning methods, Earth System Science Data, 17, 3243–3258, 2025.

Wyant, M. C., Bretherton, C. S., Rand, H. a., and Stevens, D. E.: Numerical Simulations and a Conceptual Model of the Stratocumulus to Trade Cumulus Transition, Journal of the Atmospheric Sciences, 54, 168–192, https://doi.org/10.1175/1520-0469(1997)054<0168:NSAACM>2.0.CO;2, 1997.

Yamaguchi, T., Feingold, G., and Kazil, J.: Stratocumulus to Cumulus Transition by Drizzle, Journal of Advances in Modeling Earth Systems, 9, 2333–2349, https://doi.org/10.1002/2017MS001104, 2017.

Yuan, T., Song, H., Wood, R., Mohrmann, J., Meyer, K., Oreopoulos, L., and Platnick, S.: Applying deep learning to NASA MODIS data to create a community record of marine low cloud mesoscale morphology, Atmospheric Measurement Techniques Discussions, 2020, 1–16, 2020.

Zhang, J., Zhou, X., Goren, T., and Feingold, G.: Albedo susceptibility of northeastern Pacific stratocumulus: the role of covarying meteorological conditions, Atmospheric Chemistry and Physics, 22, 861–880, 2022.

Zhou, X. and Feingold, G.: Impacts of mesoscale cloud organization on aerosol-induced cloud water adjustment and cloud brightness, Geophysical Research Letters, 50, e2023GL103 417, 2023.

Zhou, X., Bretherton, C. S., Eastman, R., McCoy, I. L., and Wood, R.: Wavelet Analysis of Properties of Marine Boundary Layer Mesoscale Cells Observed From AMSR-E, Journal of Geophysical Research: Atmospheres, 126, e2021JD034 666, 2021.